# Monitoring hemodynamic and morphologic responses to closed head injury in a mouse model using orthogonal diffuse near-infrared light reflectance spectroscopy

David Abookasis
Ariel Shochat
Marlon S. Mathews

# Monitoring hemodynamic and morphologic responses to closed head injury in a mouse model using orthogonal diffuse near-infrared light reflectance spectroscopy

**David Abookasis,a Ariel Shochat,a and Marlon S. Mathewsb**
aAriel University, Department of Electrical and Electronic Engineering, Ariel 40700, Israel
bUniversity of California Irvine, Department of Neurological Surgery, Medical Center, 101 The City Drive South, Orange, California 92868

**Abstract.** The authors' aim is to assess and quantitatively measure brain hemodynamic and morphological variations during closed-head injury (CHI) in mice using orthogonal diffuse near-infrared reflectance spectroscopy (o-DRS). CHI is a type of injury to the head that does not penetrate the skull. Usually, it is caused by mechanical blows to the head and frequently occurs in traffic accidents, falls, and assaults. Measurements of brain optical properties, namely absorption and reduced scattering coefficients in the wavelength range from 650 to 1000 nm were carried out by employing different source–detector distance and locations to provide depth sensitivity on an intact scalp over the duration of the whole experiment. Furthermore, alteration in both cortical hemodynamics and morphologic markers, i.e., scattering power and amplitude properties were derived. CHI was induced in anesthetized male mice by a weight-drop model using ~50 g cylindrical metal falling from a height of 90 cm onto the intact scalp producing an impact of 4500 g cm. With respect to baseline, difference in brain physiological properties was observed following injury up to 1 h post-trauma. Additionally, the reduced scattering spectral shapes followed Mie scattering theory was quantified and clearly shows changes in both scattering amplitude and power from baseline indicating structural variations likely from evolving cerebral edema during CHI. We further demonstrate high correlation between scattering amplitude and scattering power, with more than 20% difference in slope in comparison to preinjury. This result indicates the possibility of using the slope also as a marker for detection of structural changes. Finally, experiments investigating brain function during the first 20 min post-injury were conducted and changes in chromophore concentrations and scattering were observed. Overall, our experiments demonstrate the potential of using the proposed technique as a valuable quantitative noninvasive tool for monitoring brain physiology following CHI injury at the bedside and/or at the field. © *2013 Society of Photo-Optical Instrumentation Engineers (SPIE)* [DOI: 10.1117/1.JBO.18.4.045003]

Keywords: closed-head injury; diffuse reflectance; optical properties; absorbance; cerebral hemodynamics; scattering.

Paper 12811R received Dec. 20, 2012; revised manuscript received Mar. 6, 2013; accepted for publication Mar. 7, 2013; published online Apr. 4, 2013.

## 1 Introduction

Closed-head injuries (CHIs) are a type of traumatic brain injury in which the skull and dura mater remain intact. CHIs are usually caused by blows to the head and frequently occur in traffic accidents, falls, and assaults. CHIs can range from mild injuries to debilitating traumatic brain injuries and can lead to severe brain damage or even death.[1–6] Understanding *neurophysiologic* mechanism of brain function during CHI event can help the development of diagnostic strategies, optimize treatment, and improve therapeutic efficacy and the management of appropriate life saving care of head injuries. Computed axial tomography (CAT) and magnetic resonance imaging (MRI) are noninvasive imaging platforms used in the evaluation of head injury; however, the use of this instrument is expensive and cannot be used at the bedside for continuous monitoring.

To circumvent the above-mentioned clinical challenges, we used an alternative approach based on a diffuse light reflectance spectroscopy (DRS) paradigm because of its intrinsic sensitivity to tissue abnormalities and cerebral functions.[7–11] We reasoned that during CHI there are significant changes in the molecular concentrations of tissue chromophores, such as oxy- and deoxy-hemoglobin and water. These molecules absorb specific wavelengths of light, which alters the optical properties of the brain tissue. Hence, the goal of this research was to detect these alterations in the first critical hour of injury and quantitatively detect absolute cerebral hemodynamic and structural parameters. Compared to the above-mentioned MRI and CAT platforms, DRS is inexpensive and can be used repeatedly over a prolonged period of time with no adverse effects. It is also easy to maintain, offers high temporal resolution, and is useful for obtaining physiologic information continuously at the bedside.

DRS has been widely used so far to investigate both biochemical composition (chromophores' content)[12–15] and morphologic (structural) information[16–18] about brain tissue in research laboratories as well as in clinical environments. In its simplest configuration, DRS includes a light source, detector (spectrograph), and a pair of flexible optical fiber probes separated by a fixed distance for delivery and collection of light

Address all correspondence to: David Abookasis, Ariel University, Department of Electrical and Electronic Engineering, Ariel 40700, Israel. Tel: +972-3-9066357; Fax: +972-3-9755807; E-mail: davida@ariel.ac.il

during measurements. Light entering the tissue undergoes a combination of multiple scattering events (to the extent that it becomes randomized in direction) and absorption[19] and the reflected light from the tissue, called diffuse reflectance ($R_d$), is recorded by the detector fiber. Generally, $R_d$ signal contains information about scattering and absorption components. With this context, it was shown that separation between the source and the detection points determines the sensitivity of the measured reflectance to the absorption coefficient (large separation distances) and to the scattering coefficient (short separation).[20–22] In the context of the aforementioned basic DRS operation, we present in this paper a different arrangement for measuring the diffuse reflected light during CHI. This arrangement resembles the spatially resolved steady-state diffuse reflectance setup;[23–25] however, it differs in its simplicity, in operation, and in handling. The principle of the proposed optical setup is to monitor indirectly the absorption coefficient in the near-infrared (NIR) spectral window (650 to 1000 nm) with no constraints through two steps and then translate it into absolute concentration and saturation of hemoglobin. The steps involve direct measurement of the reduced scattering coefficient in step 1 followed by measurement of the diffuse reflected light in step 2. A diffusion equation is then used to incorporate these steps revealing the absorption coefficient at different wavelengths, which is a key for obtaining physiologic cerebral hemodynamic parameters. Even though there are several ways to model $R_d$, in this work we used the two-source diffusion-based model as described by Farrel et al.[26] The use of diffusion theory is applicable here since the source–detector separation is ~12 mm, and the brain medium is very diffuse (absorption is very low compared to the scattering). The separation of absorption coefficient from the light scattering with this arrangement enables us to quantify tissue chemical constituents (related to light absorption), such as hemoglobin concentration and oxygen saturation and structural properties (related to light scattering) accurately.

We hypothesized that our orthogonal DRS can be utilized to detect changes in tissue chromophore compositions and structural changes in the brain in response to CHI. This major hypothesis has been based upon the rationale that any variations in physiological conditions as a result of injury is expected to cause differences or alterations in optical properties, which in turn provide significant changes in $R_d$. In this pilot study, we report on our experimental investigation on a CHI mouse model for supporting the above hypothesis. To the best of our literature search, very few studies have used optical modalities to investigate CHI. One such study was published recently by Yodh's group following diffuse axonal injury, a type of CHI.[27] In that study, rotational head injuries in a neonatal piglet ($n = 18$) were conducted, and diffuse correlation spectroscopy together with DRS was used noninvasively to monitor cerebral blood flow and hemodynamic parameters (hemoglobin concentration and oxygen saturation) before injury and up to 6 h after the injury.[28] Three main differences separate our study from the same: First, we use a simpler CHI model and optical setup, second the reduced scattering coefficient is determined with the aid of power-law wavelength dependence fitting whereas in Yodh's work the scattering was assumed to be constant equal to 1/mm. To the best of our knowledge, this is the first report aimed at evaluating scattering properties changes in CHI with the help of DRS. Hence, information about the scattering power and amplitude, which are good markers of morphological

variation, can be studied now. Third, cerebral hemodynamic parameters are reported here with their absolute concentration values. Although we were not able to monitor blood flow directly, an estimation of flow variations was obtained through total hemoglobin concentration (THC). THC tracks blood flow assuming the concentration of red blood cells remains constant. In this study, CHI was induced in anesthetized male imprinting control region (ICR) mice by weight-drop model onto the intact scalp, and an optical system monitors the diffuse reflectance and light scattering before injury and up to 60 min postinjury with a 10 min gap between measurements. Concurrently, vital physiological measurements were monitored for validation purposes.

## 2  Materials and Methods

### 2.1  Animal Protocol

This study was performed in accordance with the guidelines for laboratory animal facilities and care regulation of the Institutional Animal Care and Use Committee at Ariel University Center. A total of 26 male ICR mice (age: ~12 weeks, weight: ~40 g) obtained from Harlan Laboratories were used in the experiments. Mice were divided randomly into three groups as follows: Group 1 ($n = 11$) consisted of injured mice monitored for 1 h every 10 min. Group 2 ($n = 10$) was the normal control mice that did not experience CHI. Group 3 ($n = 5$) consisted of injured mice monitored up to 20 min every 1 min. Each animal was intravenously anesthetized with a solution containing a mixture of ketamine (80 mg/kg), xylazine (20 mg/kg), and saline (NaCl, 0.9%), a combination that induced deep anesthesia and still enabled spontaneous respiration. The depth of anesthesia was ascertained by pinching of the toes or tail and by monitoring the rate of breathing. Before the experiment, the animal was placed in a prone position in a foam bed, head was fixed steadily, and mouse hair was trimmed using hair remover lotion for ease of optical fiber contact. A folded heating plate was placed under the mouse to control the body temperature at a level of 37°C, and a thermocouple rectal probe (YSI) was inserted ~2 cm to measure core body temperature. Other physiological parameters such as heart rate (HR), and arterial oxygen saturation (SpO$_2$) were monitored simultaneously using a pulse oximeter (Nonin, 8650). All mice were kept in their habitual environment until the day of the experiment. CHI was induced by a cylindrical metallic 50 g weight (pellet) dropped from a 90 cm height through a metal tube (inner diameter ~15 mm), directly onto the intact mouse scalp, producing an impact of 4500 g cm. The point of impact was between the bregma and the lambda (below the coronal suture) at the middle of the sagittal suture. Baseline reflectance measurements were obtained prior to external induction of injury. Thus each mouse serves as its own control, decreasing the number of animals required for the study. After baseline measurements were obtained, the mouse was taken out and placed under the weight-drop device orthogonal to the point of impact. Immediately postinjury, the mouse was placed back into the optical setup, and the effect of injury was studied up to 1 h post-trauma. It should be pointed out that all the mice survived the injury, and at the end of each experiment the mice were euthanized by an overdose of anesthesia. All mice underwent the same procedure. The environmental temperature was measured continuously during the experiments with digital thermometer and was $23 \pm 1$°C.

## 2.2 Weight-Drop Brain Injury Model

Weight-drop injury is a commonly used rodent model for CHI in which mechanical damage is induced indirectly to the brain through dynamic head motion, as compared to fluid percussion injury or controlled cortical contusion models where the injury to the brain is direct. Weight-drop models resemble CHI in motor vehicle accidents or falls where there is a rapid acceleration/deceleration of the head after impact to an intact skull. In the model, we used a gravitational force of a free falling weight to produce diffuse brain injury. The severity of head trauma can be varied by using different weights and/or heights of the weight-drop.[29]

## 2.3 Optical Instrumentation

Schematic of the system setup is depicted in Fig. 1(a). The setup consists of two wideband light sources, a bifurcated fiber optic probe placed in direct contact with the scalp surface,

spectrometer, pulse oximeter, rectal probe, and a computer station with control software. The lamp inside the first light source (Stockler & Yale Inc., M1000) was replaced with a broadband quartz-tungsten halogen lamp (IT, 9596-ER) to give a smooth continuum broadband spectral profile along the NIR region and stable intensity over time. Optical fiber ($D = 5$ mm) is connected to this light source placed on the scalp ~1 mm from the surface of the head. The light emanating from the brain is delivered to the spectrometer (USB4000, Ocean Optics) via bifurcated fiber with external diameter of $D = 1.3$ mm mounted on the surface of the mice scalp orthogonal to the brain surface and hence perpendicular to the first light source fiber and the brain as well. The bifurcated fiber probe comprises two separate 400 $\mu$m core diameter fibers as follows: one fiber for light delivery from a light source (HL-2000-FHSA-LL, Ocean Optics) and a second fiber for light collection to the USB4000 spectrometer. The center-to-center separation between the source and detector fibers inside the probe is approximately 400 $\mu$m, which is schematically drawn in Fig. 1(b). The receiver fiber collects
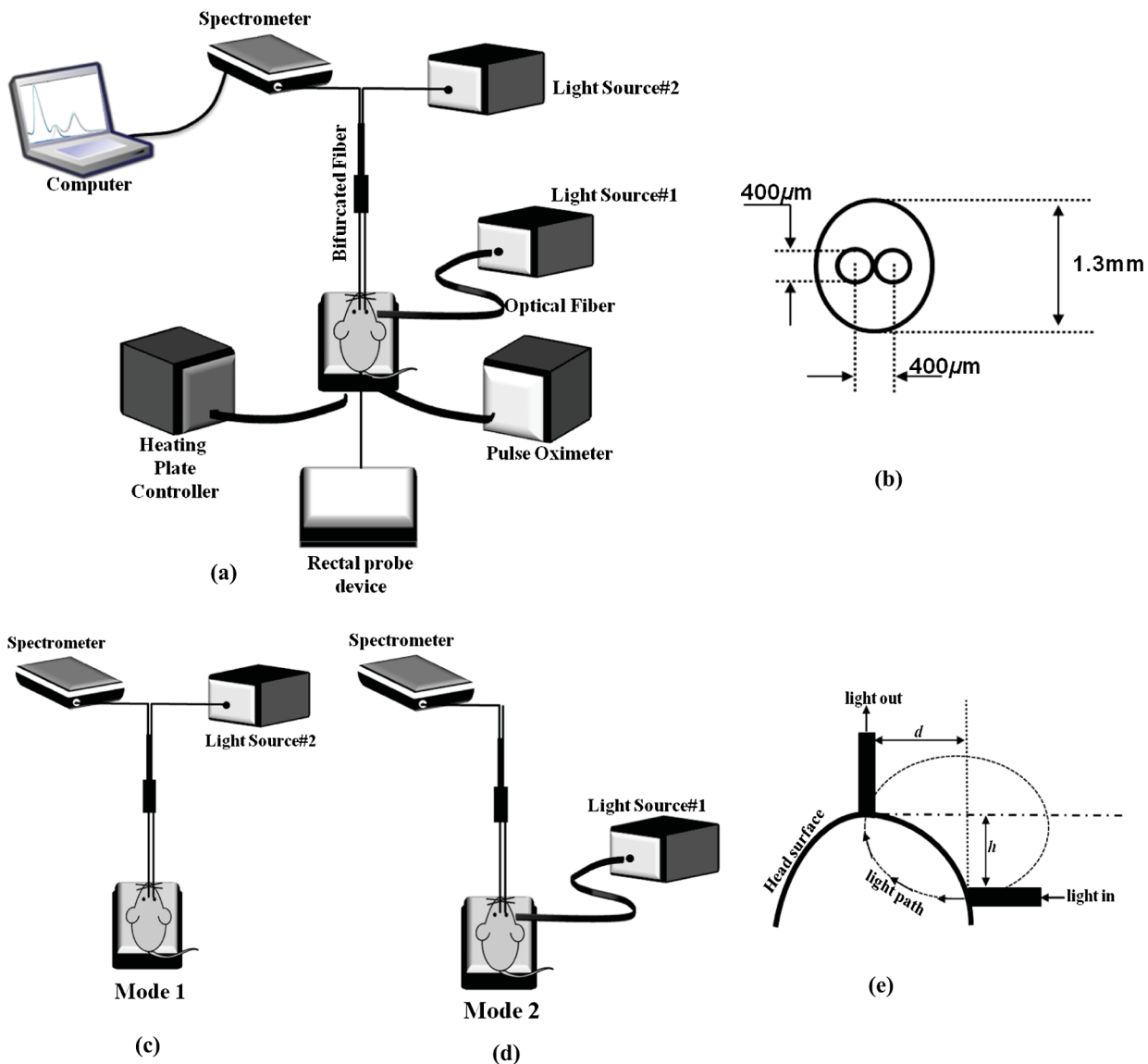


**Fig. 1** (a) Configuration of the orthogonal DRS (o-DRS) system. (b) Cross-section of the bifurcated fiber probe. (c) Schematic representation of Mode 1: scattering sensitivity. (d) Schematic representation of Mode 2: absorption sensitivity. (e) Illustration of the photon path from source No. 2 to detector in mode 2.

the diffuse reflected light in two different modes: Mode1 [Fig. 1(c)]: source–collector separation is $\rho = 400\ \mu m$ (reduced scattering coefficient,$\mu_s'$, sensitive) and Mode 2 [Fig. 1(d)]: source–collector separation is $\rho \approx 12$ mm (absorption coefficient, $\mu_a$, sensitive). Consequently, at $\rho \approx 12$ mm distance we relatively achieve deep sampling while at $\rho = 400\ \mu m$ we sample localized volumes (superficial layers). In that relation, as the distance between the source and detector decreases, we move from collection of multiply scattered light to collection of photons that experience few or single scattering events but with a lighter chance of absorption. We emphasized that once one of the light sources is operated (ON) the second source is blocked (OFF) and vice-versa. In this way of switching, we succeed in avoiding crosstalk between the two modes by sequentially operating. Hence, no overlap between measurements occurs and light scattering effect is separated from absorption. While the source-detector separation (SDS) in Fig. 1(c) is known (400 $\mu m$), the SDS in Fig. 1(e) was approximated as follows:

$$\text{SDS}_{\text{mode2}} \approx \frac{1}{4} \times 2\pi \sqrt{\frac{d^2 + h^2}{2}}. \qquad (1)$$

The distances $d$ and $h$ are depicted in Fig. 1(e). The 1/4 represents a quarter sector of the imaginary ellipse as shown in the figure. In this study, $d = 10$ mm and $h = 1$ mm reveal optical path $\approx 12$ mm. Please note that if we consider the brain as roughly spherical in shape, then the optical path (length of arc) can be calculated as $(\pi/2) \times R$, where $R$ is the mouse brain radius (~8 mm). This product gives a length of ~13 mm. In both operation modes, the reflected signal is dispersed and detected by the charge-coupled device (CCD) array in the spectrometer. The spectrometer system has a 3648-elements linear CCD array ($8 \times 200\ \mu m^2$, pixel size) with 16-bit resolution and with a spectral range from 200 to 1100 nm. Optical fibers were connected to x-y-z mechanical stage translation for position control, and care was taken to ensure full contact between the probes and the brain surface throughout the experiments. To the best of our knowledge, this is the first report of using this kind of DRS configuration, named orthogonal DRS, to evaluate brain chromophores and morphology during CHI.

## 2.4 Calibration

The acquired diffuse reflectance spectra were normalized to remove the effects of the light source spectrum, fiber attenuation, and the detector response according to the following equation:

$$\hat{R}_d(\lambda) = \frac{R_{d_{\text{msr}}}(\lambda) - R_{\text{dark}}(\lambda)}{R_{\text{whiteSTD}} - R_{\text{dark}}}, \qquad (2)$$

where $\hat{R}_d$ is the normalized diffuse reflectance in dimensionless units, $R_{d_{\text{msr}}}$ is the measured diffuse reflectance (raw spectra), $R_{\text{whiteSTD}}$ is the reflectance of a white standard sample surface (WS-1, Ocean Optics), and $R_{\text{dark}}$ is the reflectance acquired in complete darkness, and it is related to the electrical noise (thermal noise) of the CCD array. The spectrometer is programmed to automatically subtract a background reading for every reflectance measurement. The white surface provides ~100% reflectance and was used to compensate for the spectral shape of the light emitted by the lamp and the wavelength-dependent sensitivity of the detector and the optics in the detecting system. Calibration spectra were routinely measured before data

acquisition of the brain by placing the probe at a fixed distance from the white standard.

## 2.5 Derivation of Optical and Physiological Parameters

In biophotonics, light propagation in a tissue medium is described by the radiative transport equation, which can be further approximated by the diffusion equation (DE) assuming a highly scattering medium.[30–33] Numerous analytical solutions have been described in the literature over the past few years for solving the DE.[34–36] In this study, we utilize the two-source diffusion theory model derived by Farrell et al.[26] who calculate the diffuse reflectance $R_d(\rho)$ on the surface of a semi-infinite turbid medium in the diffusion approximation: (1) highly scattering media ($\mu_a \ll \mu_s'$) and (2) reflectance is measured far enough away from the light source and boundaries. The second condition implies that the observation position is sufficiently distant from the light source, i.e., $\rho \gg \text{mfp}' = (\mu_a + \mu_s')^{-1}$ (mfp is the photon transport mean free path), which is fulfilled with our system. In general, with source–detector separation larger than 10 mm standard diffusion model can be implemented while failed at short separation since photons do not travel long enough to satisfy the diffusion approximations. Under the above-mentioned conditions, Farrell et al. obtained the following steady-state diffuse reflectance expression:

$$R_d(\rho) = \frac{k_1}{(\mu_a + \mu_s')} \left\{ \left[ \mu_{\text{eff}} + \frac{1}{r_1} \right] \cdot \frac{e^{-\mu_{\text{eff}} \cdot r_1}}{r_1^2} \right. \\ \left. + \left( 1 + \frac{4}{3} k_2 \right) \left[ \mu_{\text{eff}} + \frac{1}{r_2} \right] \cdot \frac{e^{-\mu_{\text{eff}} \cdot r_2}}{r_2^2} \right\}, \qquad (3)$$

with

$$\mu_{\text{eff}} = \sqrt{3\mu_a(\mu_a + \mu_s')}, \quad r_1 = \sqrt{\rho^2 + \left( \frac{1}{\mu_a + \mu_s'} \right)^2},$$

$$r_2 = \sqrt{\rho^2 + \left[ \frac{\left( 1 + \frac{4}{3} k_2 \right)}{\mu_a + \mu_s'} \right]^2},$$

where $\rho$ is the source–detector separation, $\mu_a$ is the absorption coefficient (1/mm), $\mu_s'$ is the reduced scattering coefficient (1/mm), $\mu_{\text{eff}}$ is the effective attenuation coefficient obtained from the other two optical coefficients, and $k_1$ and $k_2$ are related to the light source intensity and the refractive index of the medium, respectively. For the large source–detector distance ($\rho \approx 12$ mm, mode 2) we use a tissue-like phantom with known optical properties over the wavelength range of 600 to 1000 nm to determine the values of $k_1$ and $k_2$ through the measured diffuse reflectance. A nonlinear least-square fit algorithm on Eq. (3) was performed to minimize the differences between the measured intensity and the intensity predicted by the model for a given set of optical properties. This fit yielded $k_1 = 2000$ and $k_2 = 1.3$. Once the model [Eq. (3)] is calibrated against the experimental reflectance [Eq. (2)], it can be applied in an inverse manner to recover the tissue optical coefficients (absorption and reduced scattering). It should be pointed out that the presented diffuse reflectance expression that appears in Eq. (3) is more adequate for semi-infinite geometry where the source and the detector are placed

on the same surface. The use of this equation as an approximation in our configuration, where the source and detector are positioned perpendicular, can lead to false results. However, with the use of a tissue-like phantom with known optical parameters, a correction can be made preventing unreliable values during measurements. Future work will be dedicated to the development of adequate mathematical expression for orthogonal source–detector position.

Studies have shown that the spectral dependence of the reduced scattering coefficient, $\mu_s'$, of tissue in the NIR region exhibits a power-law relationship as a function of wavelength, $\lambda$ given by (simplified Mie-scattering form)[37–39]

$$\mu_s'(\lambda) = A\lambda^{-\text{sp}}, \tag{4}$$

where $\mu_s' = \mu_s(1 - g)$ is the reduced scattering coefficient, $g$ is the anisotropy factor, and $\mu_s$ represents the scattering coefficient. $A$ the scattering amplitude (magnitude), which is related to the density of the scatterers (cell membrane, organelle membrane, cell nuclei, and other intracellular organelles, including the mitochondria), their distribution, and refractive index changes, whereas sp is the scattering power, which typically depends on the size of the scattering particles and defined spectral behavior of the reduced scattering coefficient.[40] Together $A$ and sp reflect changes in structural composition. As mentioned in Sec. 2.3, since light collected at small source–detector distance is sensitive to light scattering, Eq. (4) can be retrieved by collection of the diffuse light with the bifurcated probe [mode1, Fig. 1(c): light source1-OFF, light source2-ON). Since both $R_d(\rho)$ and $\mu_s'(\lambda)$ are two parameters that we measured, $k_1$ and $k_2$ found already during calibration, and $\rho$ known parameter, the absorption coefficient can be extracted now by an inverse solution to Eq. (3).

Tissue chromophores' concentration, such as oxyhemoglobin (HbO$_2$), deoxyhemoglobin (Hbr), THC (HbO$_2$ + Hbr), oxygen saturation [StO$_2$ = (HbO$_2$/THC) × 100], water concentration (H$_2$O), and lipid (fat) can be calculated now from the determined absorption values. In general, absorption coefficient is proportional to the sum of the concentrations of various chromophores presented in the medium through their molar extinction coefficients as expressed by the following Beer-Lambert law:[41]

$$\mu_a(\lambda) = \sum_{i=1}^{n} \varepsilon_i(\lambda)c_i, \tag{5}$$

where $\varepsilon_i(\lambda)$ is the molar absorption coefficient of a particular chromophore at a given wavelength $\lambda$, $c_i$ is the concentration of the chromophore (absorber), and $n$ is the number of chromophores contributing to the absorption. The molar extinction coefficient values for different chromophores are given in the literature.[42–47] The values of the above-mentioned chromophores during the entire experimental periods were calculated by an inverse solution to Eq. (5) (general solution form)

$$\vec{c} = ([\varepsilon]^T[\varepsilon])^{-1}[\varepsilon]^T\vec{\mu}_a, \tag{6}$$

where $\vec{c}$ is the chromophore concentrations vector of length $M$, $\vec{\mu}_a$ is the calculated absorption coefficients of length $N$, and $[\varepsilon]$ is the known extinction coefficients matrix with size $N \times M$. Please note that since the scalp, skull, and the dura in mice are relatively very small we assume that their influence on

the cerebral chromophore concentrations accuracy are small and chromophore estimations are mostly from the brain (gray and white matter).

### 2.6 Data Acquisition

Data acquisition, taken every 10 s along the 1 h experiment, was performed by the spectrometer. Software displays the optical reflectance in the range of 650 to 1000 nm with 2-nm increments in real time. The spectrometer interfaces to a computer via a USB 2.0 port and is controlled by a laptop computer running the Windows operating system (Intel Core, E6750 running at 2.67 GHz with 2 GB memory). Each set of data acquisition involves the measurements of replicate spectra (total of $n = 20$) at the rate of 4 Hz during single data collection session. Thus, the data acquisition time for one measurement corresponds to 5 s. These spectra are later coadded to a single average spectrum reducing the noise by a factor of $\sqrt{n}$. Before each experiment, dark and white standard sample spectrums were acquired to account for background variation as stated above [Eq. (2)]. After the DRS data acquisitions are completed, data analysis is performed off-line.

### 2.7 Data Processing

As stated in the previous section, data of the measured diffuse reflected light in the two operation modes were obtained before and after brain injury and stored in the computer for processing. Data were analyzed off-line using in-house scripts written in MatLab implementing the Eqs. (2) through (6). Prior to data analysis, the collected diffuse reflectance spectra, $\hat{R}_d$, was preprocessed to remove spectral artifacts, such as pulsations of the cortex due to respiration and heartbeat, and to eliminate high-frequency noise originated from the spectrometer. Results from processing are expressed as means ± standard error of the mean throughout the paper.

## 3 Experimental Results and Discussion

Typical results of the trends in individual brain chromophores and reduced scattering properties ($A$, sp) over time after the CHI experiment obtained from a representative mouse are illustrated in Fig. 2(a). Please note that since the spectrometer acquired spectra every 250 ms, the data presented in Fig. 2(a) is the mean value of 20 spectra corresponding to 5 s measurement. The physiological (systematic) parameters, e.g., HR, arterial oxygen saturation, and body temperature are given in Fig. 2(b) left panel. In comparison, the HR was found to significantly decrease with time after CHI. In all tested animals these vital physiological parameters expressed the same profile. The effects of CHI on brain chromophore concentrations are clearly visible in Fig. 2(a); within the first 10 min after CHI, an increase of more than 15% in the HbO$_2$, H$_2$O, and THC from the baseline measurement, respectively, was observed while the large increase was in Hbr, 55% from baseline following injury. As we progress in time, these percent changes continue to increase from the baseline. Under these conditions brain cells undergo a series of pathophysiologic changes; ultimately the injury is complicated by decreased oxygen supply as is detected by the decrease in the hemoglobin oxygen saturation (StO$_2$) by 10% from the baseline, contributing to secondary injury. It can be seen that the chromophore concentrations pre- and postinjury are distinct along the experiment duration postinjury. This observation enables one to take a representative measurement
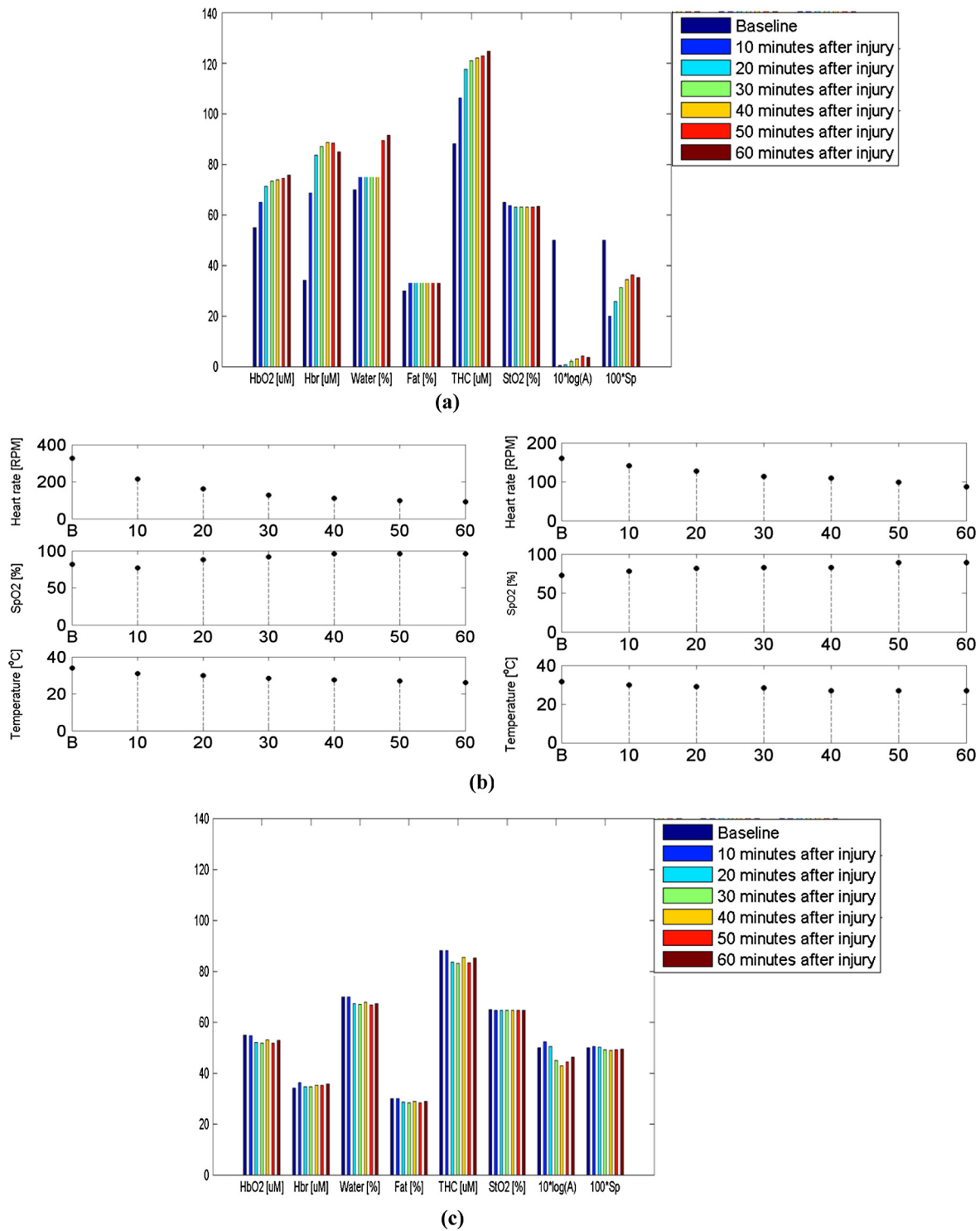
**(a)**



**(b)**



**(c)**

**Fig. 2** (a) Bar graph of chromophore concentrations and scattering properties of a representative mouse pre- and post-CHI in different time intervals. (b) Time-course of the vital physiological parameters for a control uninjured mouse (right panel) and for the representative mouse post-CHI (left panel). Note: x-axis appears in the left panel (injured mouse) represents the time post-CHI and the letter B represents the baseline. (c) Similar to (a); however, this new representative mouse did not experience injury. Please note that both *A* and sp in graphs (a) and (c) were multiplied for better visualization.

instead of long period of time to judge the physiologic status. As evidenced by directions of change in individual chromophore concentrations shown in Fig. 2(a), it can be seen that our setup is sensitive to quantitative tissue changes during CHI with time. These changes reflect the pathophysiologic state of the brain and our ability to quantify chromophore concentration during brain injury. Alteration in lipid is also observed after

CHI and may be an indication of the dysregulation of lipid metabolism within brain cells. Altered lipid metabolism is believed to contribute to secondary brain injury, which occurs after traumatic brain injury.[47,48] However, from the entire study we found less than 5% changes in lipid after CHI. Figure 2(a) further indicates variation in both scattering power (sp) and amplitude (*A*), respectively, suggesting that brain tissue

scattering properties are also effected by brain injury and metabolism and highlight the morphological changes after CHI. The decrease in the scattering power with time after injury can be explained by an increase in the average scattering particle size. This could be the result of cellular and intracellular swelling in response to acute injury as confirmed by the increase in $H_2O$ content. To match the values of $A$ and sp in the graph, these parameters were multiplied here and in the following graphs for better presentation. Because of its high values, the logarithmic value of the scattering amplitude was taken and presented throughout the paper. For comparison, in Fig. 2(c) we present the same parameters as in Fig. 2(a), at the same time interval and protocol, obtained from a control (uninjured) mouse experiment. The differences in chromophores and scattering properties between the injured and the noninjured mouse are clearly demonstrated with these figures. In the results presented in Fig. 2(c), except for $A$ and THC (slightly), no significant fluctuations over time in $HbO_2$, Hbr, $H_2O$, fat, and sp are observed, which reflects stability in measurements. The physiological parameters for the control mouse are given in Fig. 2(b) right panel. As can be seen, the biggest difference between the two is the HR value; about a twofold decrease in HR was observed for the control (anesthesia effect) while above a fourfold decrease was observed for the injured mouse. The decrease in HR in the injured mouse highlights, in addition to anesthesia, mostly the effect of the injury on the body. For completeness, the normalized reduced scattering spectra (i.e., $\mu_s'$ versus $\lambda$) measured pre- and post-CHI under different time intervals are provided in Fig. 3(a). It is interesting to observe the trend in sp (slope) after the injury; as we move from normal brain (baseline) to CHI the scattering slope becomes progressively flat with decrease of ∼60% in sp compared to the baseline and then starts to increase back in time but remain lower than its baseline value. This behavior demonstrates the morphologic changes occurring in the brain and highlights the presence of cellular swelling within brain structure.[49–52] For comparison, in Fig. 3(b), we present the normalized reduced scattering spectra as obtained from the above control noninjured mouse. As expected, the spectral behavior displayed a similar trend, and scattering slope remains the same across the time, which confirms the results of Fig. 3(a) and the possibility of using the scattering properties as a marker of tissue in pathological injury.

We repeated the above single-animal experiment in 10 mice (Group 1) with the same setup and approximately similar body weights. Figure 4 shows bar graphs of the average and standard error of both chromophore concentration and scattering properties following CHI. Please note that the standard error or the variance in chromophore and scattering properties values may represent combinations of differences in tissue chromophores in individual mice, slight fluctuation in anesthetic state, etc. In the data presented in this graph, variations in chromophores and tissue morphology ($A$, sp) are clearly observed. These findings on chromophore variations are consistent with previous observation [Fig. 2(a)] and agree well with known directions of change with brain injury.[28,53–60] As evidenced by directions of change in individual chromophores shown, it can be seen that 10 min after CHI, all the chrompohores (except $StO_2$) decreased and then showed a trend of gradually returning to the baseline level and continue to rise. This phenomenon may be related to the brain trying to overcome the stun effect of the injury. Note that the fat is the only constituent that does not change as dramatically as the others and approximately returns to its initial
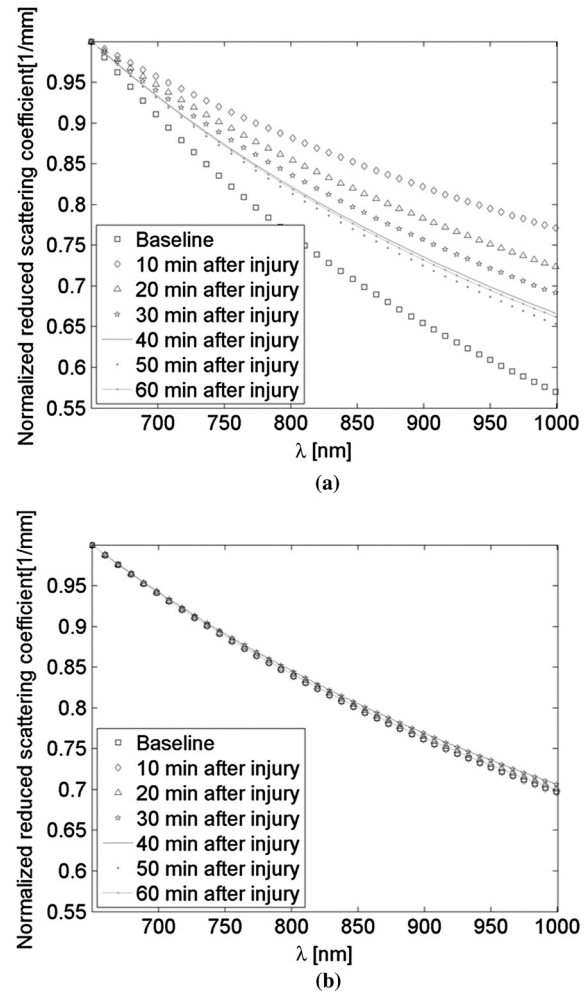


(a)



(b)

**Fig. 3** (a) Normalized reduced scattering spectra as measured by the setup of Mode 2 [Fig. 1(c)] for the injured mouse of Fig. 2(a). (b) Normalized reduced scattering spectra as measured by the setup of Mode 2 [Fig. 1(c)] for the noninjured mouse of Fig. 2(c).

value preinjury. Our findings on water content variations after injury was also observed by Xie and coworkers (see Ref. 61, Table 2, p. 5411, Group 2) using the dry/wet weight method. They reported $H_2O$ of $78.08 \pm 0.53\%$ 1 h after injury while here we report a content of $73.3 \pm 5.1\%$ post-CHI. This very slight discrepancy in results might be explained by the different setup and theoretical approaches and by variation from different experimental conditions, although the numbers themselves indicate a general agreement with our experimental results. Additionally, the alterations in scattering parameters ($A$, sp), which reflects tissue anatomical injury during CHI, to our knowledge, have not been reported. By measuring scattering amplitude and power, one can get an impression of the degree of cellular injury in terms of cell swelling (edema) and membrane damage. With this context, the scattering amplitude versus the scattering power over time is plotted in Fig. 5(a) for Group 1 and for Group 2 in Fig. 5(b), respectively. Linear regression was used to compare the change in slope. Please note, each experimental data shown in each graph corresponds to a different time-point pre- and postinjury. As seen from both panels, the correlation between $A$ and sp is higher because of the coupling between these two parameters; however, the slope of the lines become different from the injured group (slope = 0.68)
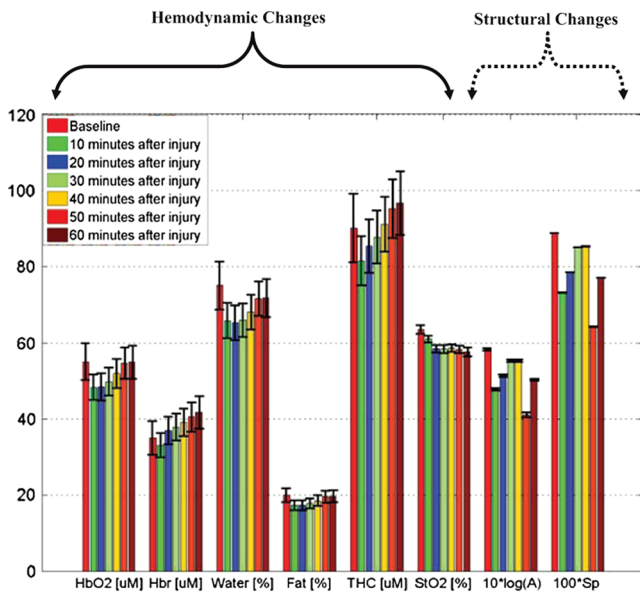
**Fig. 4** Bar graph summarizing the mean chromophore concentrations and scattering properties pre- and post-CHI in 10 mice. The results are presented as mean ± SE. Please note that both $A$ and sp were multiplied for better visualization.



**Fig. 5** (a) Graph showing scattering amplitude ($A$) versus scattering power (sp) of Group 1 obtained from Fig. 4. High correlation between $A$ and sp was obtained with $R^2 = 0.99$ and slope of 0.68. (b) Graph showing scattering amplitude ($A$) versus scattering power (sp) of Group 2 (noninjured mice). High correlation between $A$ and sp was also obtained with $R^2 = 0.95$ and slope of 0.52. It should be noted that slope was increased by more than 20% after injury. In both panels, the broken line is the best-fit linear regression fits to the data [triangles in (a) and circles in (b)].

to the noninjured group (slope = 0.52), which indicates relationship changes or an unbalanced state between scatter density ($A$) and size (sp). Therefore, the slope between $A$ and sp can also be a possible indicator for detecting anatomical structure changes in injured brain. For a short presentation at the reader's convenience, Table 1 summarizes statistical differences of specific time points of comparison in both chromophore parameters and scattering properties preinjury and 10 min and 1 h post-CHI, respectively, of Group 1.

Based on our findings, the changes in chromophore content occur within the first 10 to 20 min, which highlights the early onset of cellular swelling and brain damage contributing to secondary damage. The rapid changes occurring within the first few minutes postinjury motivated us to explore the variation in brain physiology within this time interval. The same experiment protocol, setup, and approximately similar body weights was repeated in Group 3. Time-course of brain physiology is presented in Fig. 6. Immediately following CHI, HbO$_2$, and THC levels increase while after 5 min a decrease is observed and then starts gradually to increase again. On the other hand, the Hbr level decreased and increased back 2 min after the injury. While in the previous figures a moderate decrease in StO$_2$ over the course of the 60 min postinjury period was seen, in Fig. 6 a rapid decrease in oxygen saturation was observed reflecting the progressive trauma (stun effect, secondary injury, and/or edema) to the brain in the first few minutes following CHI. As shown, 1 min from the onset of injury a rapid increase in saturation was observed. This phenomenon can be explained by the fact that over a millisecond after injury the dysfunction of intra/extracellular tissues stimulates the brain to increase oxygen supply and blood flow as expressed by increase in oxyhemoglobin and THCs (resulting in postinjury hyperemia). This finding seems to be reasonable as it indicates a larger demand for oxygen and blood following the injury. However, the ability of the brain to recuperate following a CHI period
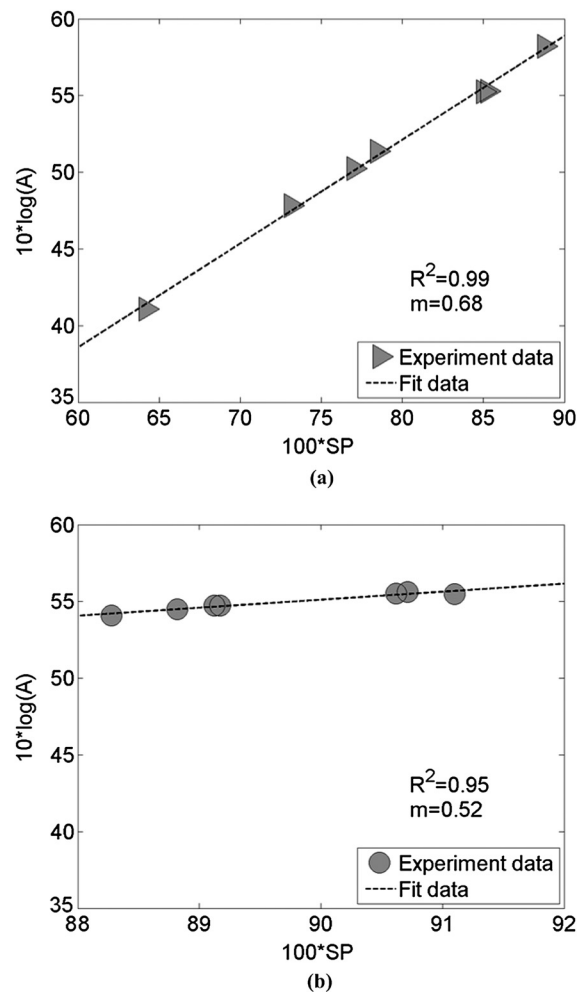
seems to decrease as the injury duration increases, which may be an indication of a damaged mechanism of autoregulation and inability of the blood supply to get to the damaged area, which is influenced from the injury duration. This implies that the damage will expand to the entire brain as injury duration becomes longer and the lack of ability of the brain for self-recovery with the increasing duration of injury. The fluctuations in chromophores also can be explained by the fact that after injury a cascade of metabolic changes promotes the development of secondary brain damage and the reaction of brain to injury can be observed by the increase and decrease in chromophore concentrations over time. Also here, the fat is the only chromophore that exhibits minor change less than 3% from its baseline. As mentioned above, the fluctuation in fat may be an indication of changes in lipid metabolism. In Fig. 7(a) and 7(b) the changes occurred in both $A$ and sp are presented. Postinjury these two parameters were increased acutely, but after 3 min they both started to decrease gradually returning toward baseline level. This turning point in time was found to be earlier

**Table 1** Statistics comparing properties pre-CHI and 10 and 60 min post-CHI of Group 1. The standard error (SE) represents combinations of variations in experimental conditions, as well as differences in tissue properties in the individual mouse.

| | Baseline | | 10 min postinjury | | 60 min postinjury | |
|---|---|---|---|---|---|---|
| | Mean $\pm$ SE | Median | Mean $\pm$ SE | Median | Mean $\pm$ SE | Median |
| HbO$_2$ ($\mu$M) | 59.06 $\pm$ 9.66 | 48.73 | 52.92 $\pm$ 5.64 | 53.77 | 59.61 $\pm$ 8.08 | 52.01 |
| Hbr ($\mu$M) | 37.36 $\pm$ 9.42 | 23.84 | 36.4 $\pm$ 6.01 | 33.63 | 44.97 $\pm$ 8.64 | 41.72 |
| THC ($\mu$M) | 94.42 $\pm$ 5.16 | 78.73 | 89.32 $\pm$ 9.01 | 87.40 | 104.58 $\pm$ 7.43 | 94.66 |
| Fat (%) | 21.48 $\pm$ 1.36 | 17.57 | 19.04 $\pm$ 1.91 | 19.19 | 21.41 $\pm$ 1.62 | 18.56 |
| StO$_2$ (%) | 64.16 $\pm$ 2.46 | 61.83 | 60.3 $\pm$ 1.83 | 60.34 | 58.43 $\pm$ 2.2 | 56.35 |
| H$_2$O (%) | 80.63 $\pm$ 10.56 | 71.94 | 74.14 $\pm$ 7.5 | 77.25 | 77.58 $\pm$ 8.82 | 74.66 |
| sp | 0.85 $\pm$ 0.1 | 0.84 | 0.68 $\pm$ 0.08 | 0.65 | 0.73 $\pm$ 0.08 | 0.77 |
| log(A) | 5.59 $\pm$ 0.69 | 5.6 | 4.47 $\pm$ 0.59 | 4.06 | 4.81 $\pm$ 0.51 | 5.04 |

than that of the chromophores (5 min) and demonstrates that scattering variations (structural changes—cell density, morphological size, and shape) occur prior to the absorption process (hemodynamics changes) following CHI. In Fig. 7(c) the scattering amplitude versus the scattering power over time is presented. As we observed previously in Fig. 5, a linear relationship with high correlation and slope of 0.68 were obtained and
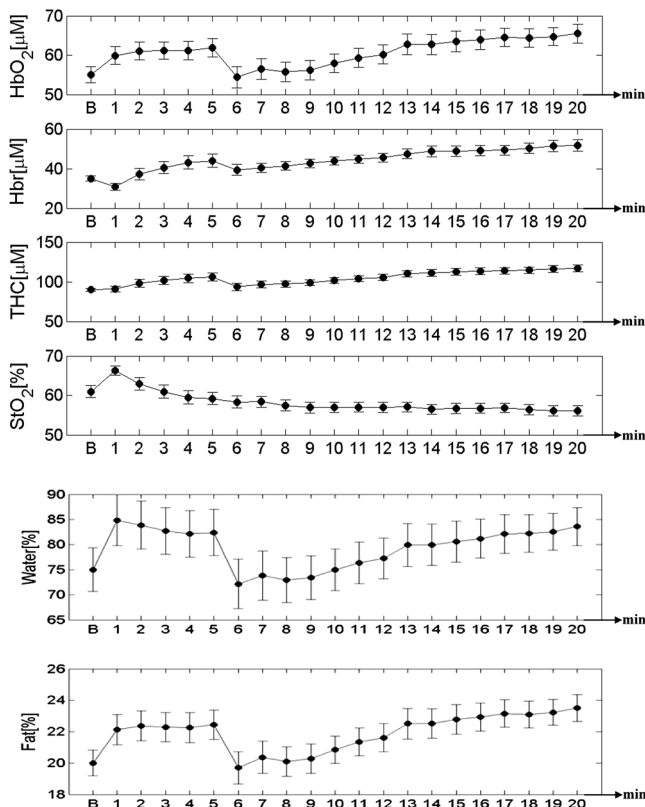


**Fig. 6** Responses of brain hemodynamic properties following CHI for Group 3. The results are presented as mean $\pm$ SE. Please note that the mice ($n = 5$) with this experiment were not included in the previous experiments. Note: the x-represents the time post-CHI and the letter B represents the baseline.
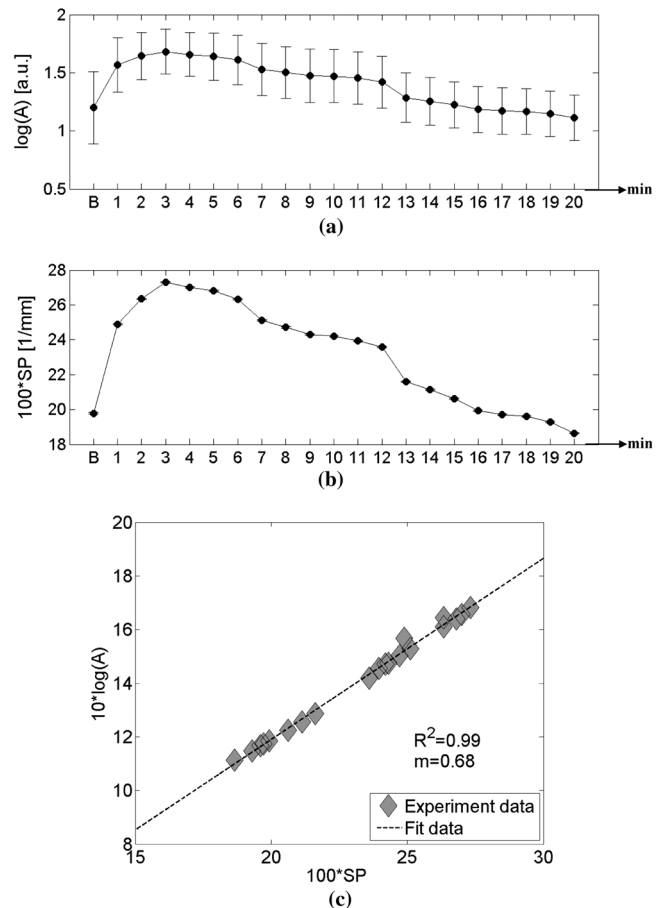


**Fig. 7** (a) Responses of brain morphology properties following CHI for Group 3. The results are presented as mean $\pm$ SE. These are the same mice group of Fig. 6. (b) Scattering amplitude ($A$) versus scattering power (sp). High correlation between the two is seen with $R^2 = 0.99$ and slope of 0.68. Note: the x-axis represents the time post-CHI and the letter B represents the baseline.

now highlight our previous conclusion that the slope can also be a good indicator for detecting anatomical disorders.

Generally speaking, CHI often creates zones of damage: a core area with severe damage and peripheral regions with moderate damage (analogous to penumbra in ischemic strokes). Because of our system configuration, the results of chromophores are influenced by the combination of both regions (volume effect) while scattering was affected mainly from the core zone. This may be a possible explanation of the difference in behavior between chromophores and structural changes and the fact that tissues with different degrees of injury will have different oxygenation states. Another source of the differences may be related to the fact that slight changes in positioning angle of the fiber probe can affect the NIR reflectance signal reading and hence the optical properties. As we mentioned in the Introduction, by assuming constant hematocrit concentration, THC can be considered as a good estimator of the concentration of blood vessels and blood flow. Since we sample diffuse zones of injury at a single measurement it is hard to conclude about the spatial brain blood flow trends. Overall, the above results and discussions monitored with our setup highlights our ability to quantify hemodynamic state and morphological variations associated with brain injury and can add valuable information and understanding regarding brain tissue in CHI suffering patients.

## 4 Conclusion

CHI is a traumatic state in which the brain is injured as a result of a mechanical blow to the head, or a sudden, violent motion that causes dynamic shifts of the brain within the skull. The current study verifies the utility and ability of o-DRS for monitoring brain physiological properties occurring during CHI. Experiments were validated on intact mice brains of a total of 26 mice (11 control, 15 injured). Our results indicated, as we hypothesized, that CHI caused changes in both optical properties of the brain tissue and consequentially cause distinctive variations over time (up to 1 h) in both chromophore concentrations and structural changes (scattering properties) in response to CHI. These results are consistent with known directions of physiological changes mentioned in the literature regarding brain trauma. In addition, we demonstrate a good correlation between the scattering amplitude (A) and scattering power (sp) and found clear change in slope in comparison to the noninjured group of mice. Although these pilot results are preliminary, we believe that the slope between A and sp can also serve as a good marker for injury. To the best of our knowledge, this is the first report aimed at evaluating scattering amplitude and power following CHI using o-DRS. The use of DRS is not new; however, the current system separates us from other groups in its configuration and our ability to separate light absorption from scattering effect in a more simple and inexpensive manner. Finally, experiments following 20 min postinjury were conducted with a gap of 1 min between measurements and results fairly resembled what we observed up to 1 h. However, a rapid decrease in oxygen saturation was observed and reflects the gradual trauma of the brain and its distress during the first minutes of injury. To sum up, the obtained results outlined here provide a proof-of-principle for the application of the aforementioned o-DRS modality in its ability to quantitatively provide information regarding the brain function following injury and potentially could be used in clinical practice. One should keep in mind that typical mean free path to an NIR absorption event in tissue is ∼10 cm, while scattering length is ∼20 to 40 $\mu$m. These numbers stand well with our setup, for example, in an adult human head where perpendicular positions of source and detector would bring very large separation (∼10 cm). Nonetheless, high sensitive detectors and the use of a supercontinuum laser source for measurement of wide spectrum will be needed in order to increase the signal-to-noise ratio. These requirements, on the contrary, are unnecessary for monitoring an infant's head because of the relative small SDS. With the advantage of the simplicity and efficiency of this technique, o-DRS can also be applicable for other medical applications in which light is used for noninvasive diagnosis.

## References

1. J. T. E. Richardson, *Clinical and Neuropsychological Aspects of Closed Head Injury*, 2nd ed., Psychology Press, East Sussex, UK (2002).
2. R. L. Rodnitzky and M. Meier, "Neurobehavioral consequences of closed head injury," *Arch. Neurol.* **39**(10), 675–676 (1982).
3. E. Arcia and C. T. Gualtieri, "Neurobehavioural performance of adults with closed-head injury, adults with attention deficit, and controls," *Brain Inj.* **8**(5), 395–404 (1994).
4. A. Aronson, "Laryngeal-phonatory dysfunction in closed head injury," *Brain Inj.* **8**(8), 663–665 (1994).
5. O. Zohar et al., "Closed-head minimal traumatic brain injury produces long-term cognitive deficits in mice," *J. Neurosci.* **118**(4), 949–955 (2003).
6. A. Milman et al., "Mild traumatic brain injury induces persistent cognitive deficits and behavioral disturbances in mice," *J. Neurotrauma.* **22**(9), 1003–1010 (2005).
7. W. C. Lin et al., "Diffuse reflectance spectroscopy for *in vivo* pediatric brain tumor detection," *J. Biomed. Opt.* **15**(6), 061709 (2010).
8. J. Antonsson et al., "Diffuse reflectance spectroscopy measurements for tissue-type discrimination during deep brain stimulation," *J. Neural. Eng.* **5**(2), 185–190 (2008).
9. J. G. Rodriguez et al., "Feasibility of using diffuse reflectance spectroscopy for the quantification of brain edema," *Proc. SPIE* **4241**, 88–97 (2001).
10. D. M. Hueber et al., "Non-invasive and quantitative near-infrared hemoglobin spectrometry in the piglet brain during hypoxic stress, using a frequency-domain multidistance instrument," *Phys. Med. Biol.* **46**(1), 41–62 (2001).
11. B. Hallacoglu et al., "Cerebral perfusion and oxygenation are impaired by folate deficiency in rat: absolute measurements with noninvasive near-infrared spectroscopy," *J. Cereb. Blood. Flow Metab.* **31**(6), 1482–1492 (2011).
12. R. Nachabé et al., "Estimation of biological chromophores using diffuse reflectance spectroscopy: benefit of extending the UV-VIS wavelength range to include 1000 to 1600 nm," *Biomed. Opt. Exp.* **1**(5), 1433–1442 (2010).
13. J. Choi et al., "Noninvasive determination of the optical properties of adult brain: near-infrared spectroscopy approach," *J. Biomed. Opt.* **9**(1), 221–229 (2004).
14. J. Zhao et al., "*In vivo* determination of the optical properties of infant brain using frequency-domain near-infrared spectroscopy," *J. Biomed. Opt.* **10**(2), 024028 (2005).
15. H. Sato et al., "Intersubject variability of near infrared spectroscopy signals during sensorimotor cortex activation," *J. Biomed. Opt.* **10**(4), 44001 (2005).
16. F. Bevilacqua et al., "*In vivo* local determination of tissue optical properties: applications to human brain," *Appl. Opt.* **38**(22), 4939–4950 (1999).
17. A. N. Yaroslavsky et al., "Optical properties of selected native and coagulated human brain tissues *in vitro* in the visible and near infrared spectral range," *Phys. Med. Biol.* **47**(12), 2059–2073 (2002).
18. D. Abookasis et al., "Diffuse near-infrared reflectance spectroscopy during heatstroke in a mouse model: a pilot study," *J. Biomed. Opt.* **17**(10), 027001 (2012).
19. V. V. Tuchin, *Tissue Optics: Light Scattering Methods and Instruments for medical Diagnosis*, 2nd ed., SPIE Press, Bellingham, WA (2007).
20. G. Kumar and J. M. Schmitt, "Optimal probe geometry for near-infrared spectroscopy of biological tissue," *Appl. Opt.* **36**(10), 2286–2293 (1997).

21. M. Johns et al., "Determination of reduced scattering coefficient of biological tissue from a needle-like probe," *Opt. Express* **13**(13), 4828–4842 (2005).

22. A. Kim et al., "Fiberoptic reflectance probe with multiple source-collector separations to increase the dynamic range of derived tissue optical absorption and scattering coefficients," *Opt. Express* **18**(6), 5580–5594 (2010).

23. A. Kienle et al., "Spatially resolved absolute diffuse reflectance measurements for noninvasive determination of the optical scattering and absorption coefficients of biological tissue," *Appl. Opt.* **35**(13), 2304–2314 (1996).

24. J. Swartling, J. S. Dam, and S. Andersson-Engels, "Comparison of spatially and temporally resolved diffuse-reflectance measurement systems for determination of biomedical optical properties," *Appl. Opt.* **42**(22), 4612–4620 (2003).

25. M. Larsson, H. Nilsson, and T. Strömberg, "*In vivo* determination of local skin optical properties and photon path length by use of spatially resolved diffuse reflectance with applications in laser Doppler flowmetry," *Appl. Opt.* **42**(1), 124–134 (2003).

26. T. J. Farrell and M. S. Patterson, "A diffusion theory model of spatially resolved, steady-state diffuse reflectance for the noninvasive determination of tissue optical properties *in vivo*," *Med. Phys.* **19**(4), 879–888 (1992).

27. D. H. Smith, D. F. Meaney, and W. H. Shull, "Diffuse axonal injury in head trauma," *J. Head. Trauma. Rehabil.* **18**(4), 307–316 (2003).

28. C. Zhou et al., "Diffuse optical monitoring of hemodynamic changes in piglet brain with closed head injury," *J. Biomed. Opt.* **14**(3), 034015 (2009).

29. M. A. Flierl et al., "Mouse closed head injury model induced by a weight-drop device," *Nat. Protoc.* **4**(9), 1328–1337 (2009).

30. R. C. Haskell et al., "Boundary conditions for the diffusion equation in radiative transfer," *J. Opt. Soc. Am. A* **11**(10), 2727–2741 (1994).

31. T. Khan and H. Jiang, "A new diffusion approximation to the radiative transfer equation for scattering media with spatially varying refractive indices," *J. Opt. A: Pure Appl. Opt.* **5**(2), 137–141 (2003).

32. V. Venugopalan, J. S. You, and B. J. Tromberg, "Radiative transport in the diffusion approximation: an extension for highly absorbing media and small source-detector separations," *Phys. Rev. E.* **58**(2), 2395–2406 (1998).

33. A. D. Kim and A. Ishimaru, "Optical diffusion of continuous-wave, pulsed, and density waves in scattering media and comparisons with radiative transfer," *Appl. Opt.* **37**(22), 5313–5319 (1998).

34. M. Machida et al., "Diffusion approximation revisited," *J. Opt. Soc. Am. A* **26**(5), 1291–1300 (2009).

35. A. D. Kim, "Correcting the diffusion approximation at the boundary," *J. Opt. Soc. Am. A* **28**(6), 1007–1015 (2011).

36. C. Chai et al., "Improved steady-state diffusion approximation with an anisotropic point source and the δ-Eddington phase function," *Appl. Opt.* **46**(21), 4843–4851 (2007).

37. H. J. Van Staveren et al., "Light scattering in intralipid-10% in the wavelength range of 400-1100 nm," *Appl. Opt.* **30**(31), 4507–4514 (1991).

38. R. Graaff et al., "Reduced light-scattering properties for mixtures of spherical particles: a simple approximation derived from Mie calculations," *Appl. Opt.* **31**(10), 1370–1376 (1992).

39. J. R. Mourant et al., "Predictions and measurements of scattering and absorption over broad wavelength ranges in tissue phantoms," *Appl. Opt.* **36**(4), 949–957 (1997).

40. X. Wang et al., "Approximation of Mie scattering parameters in near-infrared tomography of normal breast tissue *in vivo*," *J. Biomed. Opt.* **10**(5), 051704 (2005).

41. D. A. Boas, C. Pitris, and N. Ramanujam, "Light scattering spectroscopy," Chapter 8 in *Handbook of Biomedical Optics*, pp. 166–167, CRC Press, Boca Raton, FL (2011).

42. S. Wray et al., "Characterization of the near infrared absorption spectra of cytochrome aa3 and haemoglobin for the non-invasive monitoring of cerebral oxygenation," *Biochim. Biophys. Acta* **933**(1), 184–192 (1988).

43. G. M. Hale and M. R. Querry, "Optical constants of water in the 200-nm to 200-$\mu$m wavelength region," *Appl. Opt.* **12**(3), 555–563 (1973).

44. C. Eker, "Optical characterization of tissue for medical diagnostics," Ph.D. Thesis, Lund Institute of Technology (1999).

45. W. G. Zijlistra, A. Buursma, and O. W. V. Assendelft, *Visible and Near Infrared Absorption Spectra of Human and Animal Haemoglobin: Determination and Application*, VSP, AH Zeist, Netherlands (2000).

46. R. L. P. van Veen et al., "Determination of VIS-NIR absorption coefficients of mammalian fat, with time and spatially resolved diffuse reflectance and transmission spectroscopy," in *Biomedical Topical Meeting*, Optical Society of America, Washington, DC (2004).

47. R. M. Adibhatla and J. F. Hatcher, "Altered lipid metabolism in brain injury and disorders," *Subcell. Biochem.* **49**, 241–268 (2008).

48. R. M. Adibhatla, J. F. Hatcher, and R. J. Dempsey, "Lipids and lipidomics in brain injury and diseases," *J. Am. Assc. Pharm. Sci.* **8**(2), E314–E321 (2006).

49. A. Marmarou, "Pathophysiology of traumatic brain edema: current concepts," *Acta. Neurochir. Suppl.* **86**, 7–10 (2003).

50. J. J. Donkin and R. Vink, "Mechanisms of cerebral edema in traumatic brain injury: therapeutic development," *Curr. Opin. Neurol.* **23**(3), 293–299 (2010).

51. D. Abookasis et al., "Using NIR spatial illumination for detection and mapping chromophore changes during cerebral edema," *Proc. SPIE* **6842**, 68422U (2008).

52. A. S. Gill et al., "Early optical detection of cerebral edema *in vivo*," *J. Neurosurg.* **114**(2), 470–477 (2011).

53. E. M. C. Hillman, "Optical brain imaging *in vivo*: techniques and applications from animal to man," *J. Biomed. Opt.* **12**(5), 051402 (2007).

54. D. Abookasis et al., "Imaging cortical absorption, scattering, and hemodynamic response during ischemic stroke using spatially modulated near-infrared illumination," *J. Biomed. Opt.* **14**(2), 024033 (2009).

55. Y. Jia et al., "*In vivo* optical imaging of revascularization after brain trauma in mice," *Microvasc. Res.* **81**(1), 73–80 (2011).

56. J. P. VanHouten et al., "Imaging brain injury using time-resolved near infrared light scanning," *Pediatr. Res.* **39**(3), 470–476 (1996).

57. L. J. Johnson, D. F. Hanley, and N. V. Thakor, "Optical light scatter imaging of cellular and sub-cellular morphology changes in stressed rat hippocampal slices," *J. Neurosci. Methods* **98**(1), 21–31(2000).

58. W. Li et al., "The in-vivo monitoring method for traumatic brain injury of mouse based on near-infrared light intensity," *Proc. SPIE* **8207**, 82071N (2012).

59. P. B. Jones et al., "Simultaneous multispectral reflectance imaging and laser speckle flowmetry of cerebral blood flow and oxygen metabolism in focal cerebral ischemia," *J. Biomed. Opt.* **13**(4), 044007 (2008).

60. M. Calderon-Arnulphi et al., "Detection of cerebral ischemia in neurovascular surgery using quantitative frequency-domain near-infrared spectroscopy," *J. Neurosurg.* **106**(2), 283–290 (2007).

61. J. Xie et al., "Minimally invasive assessment of the effect of mannitol and hypertonic saline therapy on traumatic brain edema using measurements of reduced scattering coefficient($\mu$s′)," *Appl. Opt.* **49**(28), 5407–5414 (2010).